Validating Simulated Mountain Wave Impacts on Hub-Height Wind Speed Using SoDAR Observations

Geng Xia[1], Caroline Draxl[1], Ajay Raghavendra[2], Julie K. Lundquist[1,3]

[1]National Renewable Energy Laboratory, Golden, CO 80401 USA
[2]Department of Atmospheric and Environmental Sciences, University at Albany, Albany, NY, USA
[3]Department of Atmospheric and Oceanic Sciences, University of Colorado Boulder, Boulder, CO 80302 USA

Correspondence to Geng Xia (gxia@nrel.gov)

Submitted to *Renewable Energy*

Abstract

The ascent of stably stratified air over a mountain barrier can trigger the generation of mountain waves. Mountain waves occur frequently over the Columbia River Gorge in western North America and can impact wind power generation over the area. Therefore, predicting the details of mountain waves events (e.g., dominant wavelength, timing, and duration) can be very valuable for the wind energy community. In this study, the ability of the Weather Research and Forecasting (WRF) model to simulate mountain waves and their impact on hub-height wind speed is investigated. Our results suggest that the WRF model has moderate skill in simulating observed mountain wave. Further, given WRF predictions of wavelength range and wave period, the Fast Fourier Transform can calculate the simulated mountain wave impact on hub-height wind speed. The resulting wind speeds agree well with SoDAR observations in terms of both magnitude and pattern. Finally, for the simulated cases, WRF consistently predicts impacts of significant mountain wave events about an hour earlier than the actual observations. The sensitivities as well as uncertainties associated with our methodology are discussed in detail.

Keywords: Mountain wave; WRF modeling; Wind forecasting; Fourier filtering

1. Introduction

In the recent decade, the installed wind power in the United States has experienced a dramatic growth, exceeding hydropower as the nation's largest renewable energy source (U.S. Department of Energy, 2018a). A large amount of wind energy (~60 GW) is installed in the complex terrain, such as mountain regions (https://eerscmap.usgs.gov/uswtdb/). However, the complexity of the atmospheric flow over such regions makes it challenging to predict the timing and magnitude of wind speeds (Emeis et al. 2018; Serafin et al. 2018; Veers et al. 2019; Lehner et al. 2018; van den Bossche et al. 2019). Therefore, improving our understanding of complex-terrain meteorology has become a critical need for the advancement of wind energy.

In 2015, the U.S. Department of Energy (DOE) initiated a 4-year study, the Second Wind Forecast Improvement Project(WFIP2), to improve the representation of boundary layer physics and related processes in mesoscale models for better forecasting of wind and wind power over the complex terrain (Shaw et al. 2019; Wilczak et al. 2019; Olson et al. 2019). The Columbia River basin in the Pacific Northwest, home to more than 4 GW of wind energy production, was selected as the study region because it is an exceptional natural observatory for studying meteorological phenomena associated with complex terrain.

The Cascade Range, which is situated west of the Columbia River Basin, is a major mountain range in western North America, extending from southern British Columbia through Washington to Northern California. Because of the region's prevailing westerly wind, the Cascade Range posts an obstacle that impacts and modifies air flow downwind. Depending on atmospheric conditions, various atmospheric phenomena, such as gap flows, mountain waves, and downslope wind, can occur with varying intensity and on many different temporal and spatial scales (Wilczak et al. 2019). All of these present a unique challenge to short-term wind and wind energy forecasting in the region.

When a stably stratified airflow ascends over a topographic barrier, such as the Cascade Range, mountain waves tend to be generated due to buoyancy perturbation. In fact, multiple significant mountain wave events were observed during the WFIP2 field campaign, particularly during the winter and spring season. In general, there are two kinds of mountain wave, the vertically propagating waves and trapped lee waves (Durran 2003; 2015). Trapped lee waves tend to have more impacts on wind energy because they usually occur at the low levels of the troposphere and their horizontal wavelength (5~ 35 km; AMS Glossary) is about the size of a wind farm plant. The crests of these waves often contain wave clouds that can be very striking in satellite images (Feltz et al. 2009; Li et al. 2017). Since these mountain waves are trapped within the stable layer, they may dissipate slowly and can propagate downstream, presenting a significant challenge to wind power generation as well as low-altitude aviation.

To our best knowledge, Wilczak et al. (2019) is the first study to document to the impact of mountain waves on wind energy production. They confirmed that wave activities from the observed mountain wave event on November 12th 2016 coincide with wind turbine power output variability. In a subsequent study, Draxl et al. (2020) conducted a high-resolution numerical simulation, which successfully reproduced a mountain wave event on September 24th 2016. Their results indicated that the simulated mountain waves occurred about 1 hour earlier than the observed, and that the wavelength and periods of the mountain wave event were well forecast. However, their study analyzed just one mountain wave event. From an operational forecasting perspective, knowing when any significant mountain waves will occur can be very valuable for the wind energy sector. Therefore, the purpose of this study is to further investigate whether mesoscale model simulations can accurately predict the timing, wavelengths, and wave period of the mountain wave events by conducting multiple mountain wave simulations.

The remainder of the paper is divided into four sections. The data and methods employed are described in Section 2. The simulated mountain wave activities from the model simulations are analyzed and validated with observations in detail in Section 3. The uncertainties associated with our methodology are discussed in Section 4, followed by the conclusions in Section 5.

2. Data and methodology

2.1 Selection of mountain wave cases

Each week throughout the WFIP2 field campaign (October 2015 to March 2017), scientists and wind energy forecasters reviewed the daily weather in the region and wrote a brief synopsis in an event log (Wilzcak et al. 2019) to assess important weather phenomena that impacted wind power generation. In total, about 190 mountain wave cases were identified, 16 of which were identified as having potential significance for renewable energy purposes. Therefore, predicting and forecasting those significant mountain wave events will be valuable for the wind energy sector. In this study, 3 of those 16 significant mountain wave cases, which occurred on November 11th 2015 (20151111), February 14th 2016 (20160214) and April 04th 2016 (20160404) were selected. The first two cases were the only two cases where wave clouds were present during the Moderate Resolution Imaging Spectroradiometer (MODIS) measurement time, while the third case was chosen as a representative case with no wave clouds.

2.2 Disentangling simulated mountain wave signals from the total wind field using spectral method

Since numerical model simulation provides the three-dimensional (time, latitude and longitude) structure of the simulated wind field, the simulated mountain wave signals on the wind field can be extracted by using the Fourier filtering, which is a common method to attenuate or amplify a specific frequency of signal (Bergland GD. 1969; Borkowski J. 1969; Jenkins GM and Watts DG. 1968; Panofsky HA and Brier GW. 1968; Stull RB. 1988; Raghavendra et al. 2019; Sussman et al. 2020).

In this study, a band-pass filter wavelength ranges from 8 to 20 km and wave periods from 1 to 4 hours were applied to capture mountain waves (e.g., Draxl et al. 2020). These wavelengths and wave periods are typical for trapped lee waves which occurred over the WFIP2 study region (Wilczak et al. 2019; Draxl et al. 2020). At the latitude of Van Gilder and Prineville (Fig. 1), simulated hub-height wind speed at each time step was first reconstructed using the wavelength constraints. Next, the hub-height wind field at Prineville and Van Gilder were reconstructed using the wave period constraints. Thus, the resulting hub-height wind speed is constrained by both the wavelength and wave period selection. The resulting power variance associated with the targeted wavelengths determines the duration of the significant mountain wave events. In this study, a mountain wave event was considered significant when the power variance explained by the targeted wavelength range exceeded 25 % of the total variance for at least 3 hours. The uncertainties associated with the wavelength, wave period, power variance threshold and wave duration are discussed in detail in Section 4.

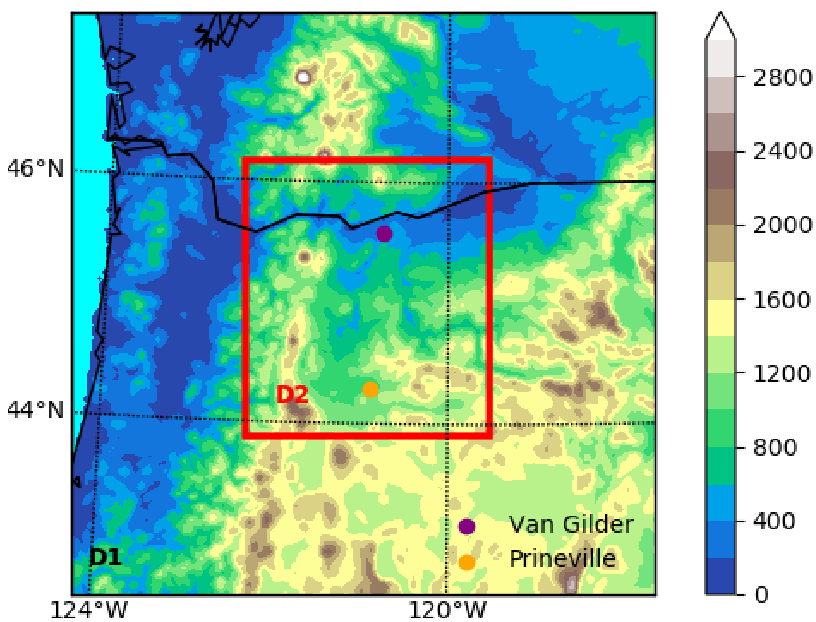

Figure 1: Topography (meters) over the WRF Model domain. The purple and orange dots indicate the geographical locations of Van Gilder and Prineville.

2.3 Model and simulation design

The Weather Research and Forecasting model (WRF) version 4.1.2 is used to conduct the model simulation in this study (Skamarock and Klemp., 2008; Powers et al., 2017). The model configuration (physical options) is summarized in Table 1. Both the boundary and initial conditions are from the ERA-interim dataset (https://rda.ucar.edu/datasets/ds627.0/; Dee et al., 2011). The topography, soil characteristics, and MODIS-based land cover data are obtained from the WRF standard dataset.

Table 1: Summary of WRF Model Configuration

Shortwave	Rapid Radiative Transfer Model for GCMs (Iacono et al. 2008)
Longwave	Rapid Radiative Transfer Model for GCMs (Iacono et al. 2008)
Microphysics	Thompson aerosol-aware (Thompson et al. 2008; Thompson and Eidhammer. 2014)
Boundary Layer	Yonsei University scheme (Hong et al. 2006)
Land Surface	Noah Land Surface Model (Chen and Duhia. 2001)
Surface Layer	Revised MM5 (Jimenez et al. 2012)

The simulations are performed with two nested domains centered on the WFIP2 campaign region (Fig. 1). The outer domain consists of 181 x 181 grid points with a horizontal spacing of 3 km and the inner domain consists of 301 x 341 grid points with a grid spacing of 750 m (Bianco et al. 2019). Note that cumulus convection is treated explicitly for both domains. A vertically stretched grid consisting of 44 levels is employed with finer resolution at lower levels (13 within the lowest 200m) and coarser resolution at higher levels.

Each mountain wave simulation is initialized 12 hours before the actual event date and then run for 60 hours (Xia et al. 2017; 2019). The first 12 hours are discarded as spinup, and only data from the two days after are used for analysis.

2.4 Observation data

2.4.1 MODIS Data

Mountain waves often manifest with wave clouds. The MODIS Version 6 surface spectral reflectance (MOD09GQ; Vermote et al. 2015) at 250 m resolution was used to examine cloud conditions. Figure 2a), 2b) and 2c) show the cloud images at 18:30 UTC for all the three cases. Wave clouds are present for the mountain wave cases on 20151111 and 20160214. However, only scatter clouds appeared on 20160404. Figure 2d), 2e) and 2f) show the spatial pattern of hub-height wind speed at the exact same time from the three respective model simulations respectively. Even though it is not a direct comparison, mountain waves can be seen in the simulated wind field as similarly spaced oscillating strips of high and low wind speeds (Wilczak et al. 2019; Draxl et al. 2020). Qualitatively, the wave activities as well as their geographical locations are successfully simulated for the 20151111 and 20160214 cases, but no evident wave activities are simulated for the 20160404 case. Overall, the simulated wave activities agree well with the satellite observations.

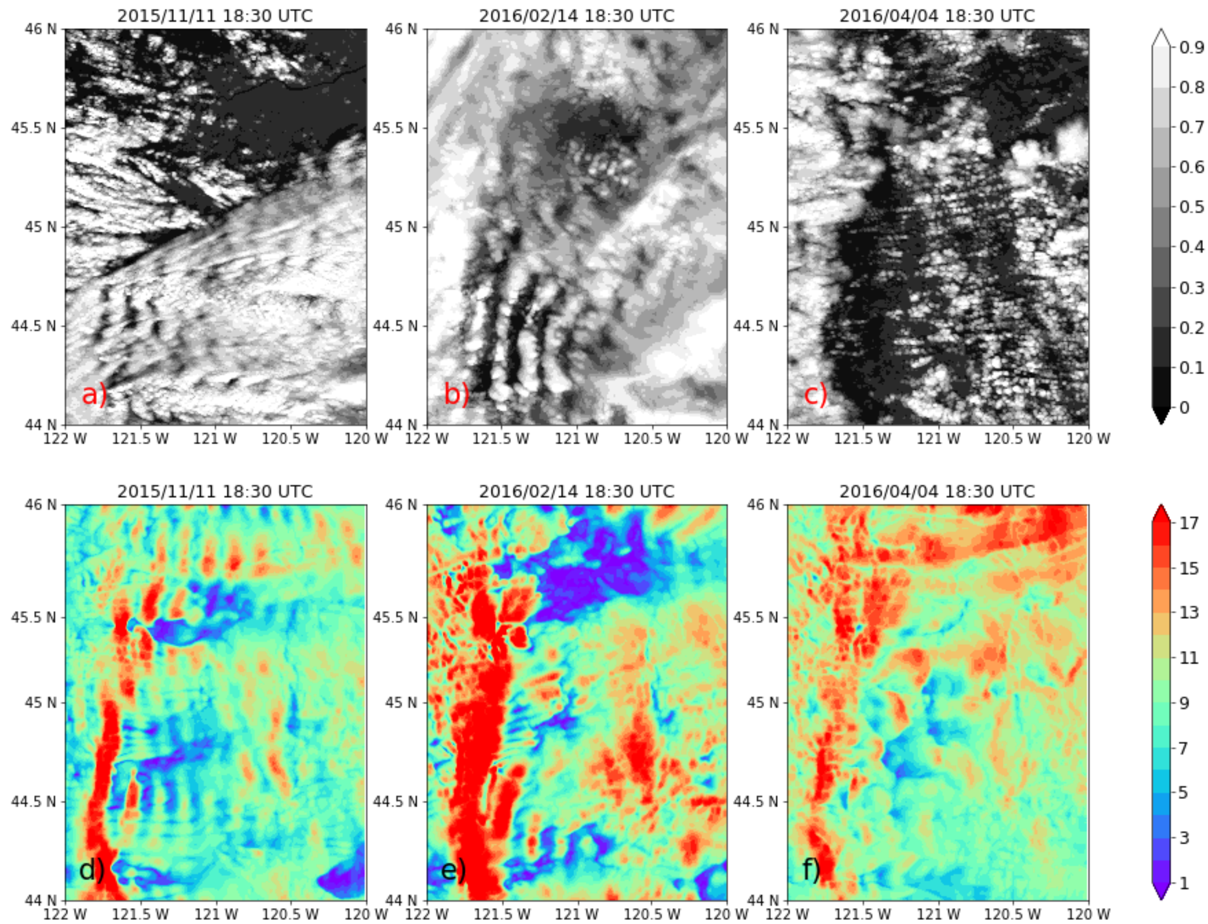

Figure 2: MODIS images and simulated wind speeds at 100 m from the three case studies: a) MODIS Terra satellite reflectance (W.m^{-2}.μm^{-1}.sr^{-1}) on 20151111 at 18: 30 UTC; b) same as a) but on 20160214 at 18: 30 UTC; c) same as a) but on 201600404 at 18: 30 UTC; d) spatial pattern of simulated wind speeds at 100 m (m.s^{-1}) on 20151111 at 18: 30 UTC; e) same as d) but on 20160214 at 18: 30 UTC; f) same as d) but on 20160404 at 18: 30 UTC.

2.4.2 SoDAR Wind profiler

In total, there are 13 SoDAR wind profilers situated in Domain 2 (Fig. 1). The one in Prineville is the only wind profiler on the southern side of the domain while the rest are clustered around 45.6^{o}N latitude. The SoDAR in Van Gilder is chosen as the representative wind profiler for the northern side of the domain because it is located on the center of the other 12. Therefore, the SoDAR wind profilers from the Van Glider and Prineville (Fig. 1) are used to validate the simulated mountain wave activities. At Van Glider, a Vaisala Triton wind profiler (Vaisala, 2015) is used whereas at Prineville, an atmospheric science crop (ASC) wind profiler (http://www.minisodar.com/sodar/) is used. Both profilers measure wind speed and direction at heights from 40 m to 200 m above the ground at every 10 minutes at Van Glider and every 15 minutes at Prineville. The quality controlled SoDAR data are stored on the Data Archive and Portal (https://a2e.energy.gov/about/dap). Since this study focuses on renewable wind energy, only wind speed at hub-height,100 m above ground level (AGL), is used for the analysis.

3. Results

3.1 Determining mountain wave activities from model simulations

Figure 3 shows the timeseries of the simulated power variance (%) explained by the targeted wavelengths (8 ~ 20 km) from the three mountain wave simulations. Figure 3a) and 3b) shows the timeseries at Van Gilder and Prineville from 20151111 and 20160214 whereas Figure 3c) and 3d) shows the similar plots but from 20160404. Based on our definition of a significant mountain wave event (Section 2.1), four significant mountain wave events are identified from the model simulations. The first event occurs on November 11th, 2015, from 18 UTC to 22 UTC at Van Gilder. The second event occurs on February 14th, 2016, from 21 UTC to 02 UTC the next day at Prineville. The third event occurs on April 05th, 2016, from 02 UTC to 09 UTC at Van Gilder whereas the fourth event occurs on April 05th, 2016, from 01 UTC to 05 UTC at Prineville. Note that the results at Prineville and Van Gilder from 20151111 and 20160214 are not included because there were not any significant mountain wave events being simulated.

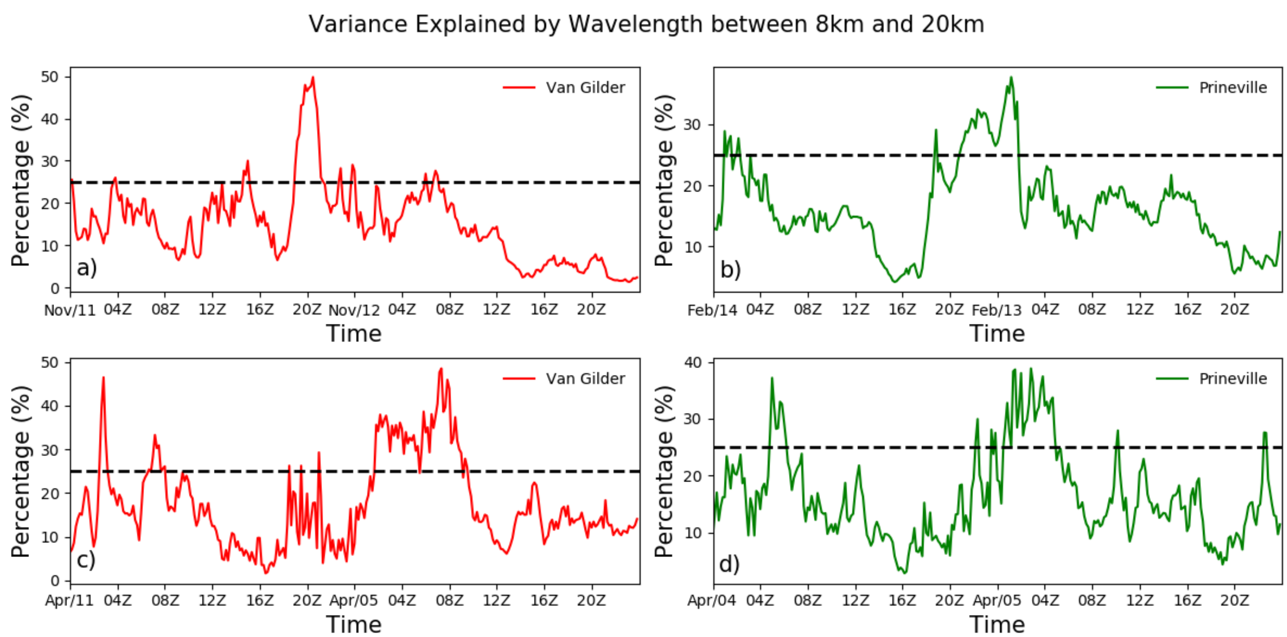

Figure 3: Timeseries of the simulated power variance explained by the targeted wavelengths (8 ~20 km) from the three mountain wave simulations: a) Van Gilder, 20151111; b) Prineville, 20160214; c) Van Gilder, 20160404; and d) Prineville, 20160404. The black dashed line indicates the 25 % threshold.

To further illustrate these four identified mountain wave events, Figure 4 indicates the Hovmöller diagram of the simulated power variance with respect to wavelength at the latitude of Van Glider and Prineville from all four events. About 75 % of the atmospheric variabilities are explained by the large wave patterns (> 20 km). These large-scale wave activities, which last the entire simulation period, are mainly associated with the background synoptic conditions. Within our targeted mountain wave wavelength range (8 ~ 20 km), there are significant mountain wave activities occurring during the identified event periods (Fig. 3). Furthermore, the simulated mountain waves from each event differ in terms of wave characteristics. For instance, the simulated mountain wave event on 20151111 manifests mostly as a single wavelength whereas the other mountain wave events are associated with a partial or entire wavelength spectrum between 8 and 20 km. For wavelengths shorter than 8 km, the associated power variance is small, indicating negligible impacts from the high-frequency waves on the overall hub-height wind speed.

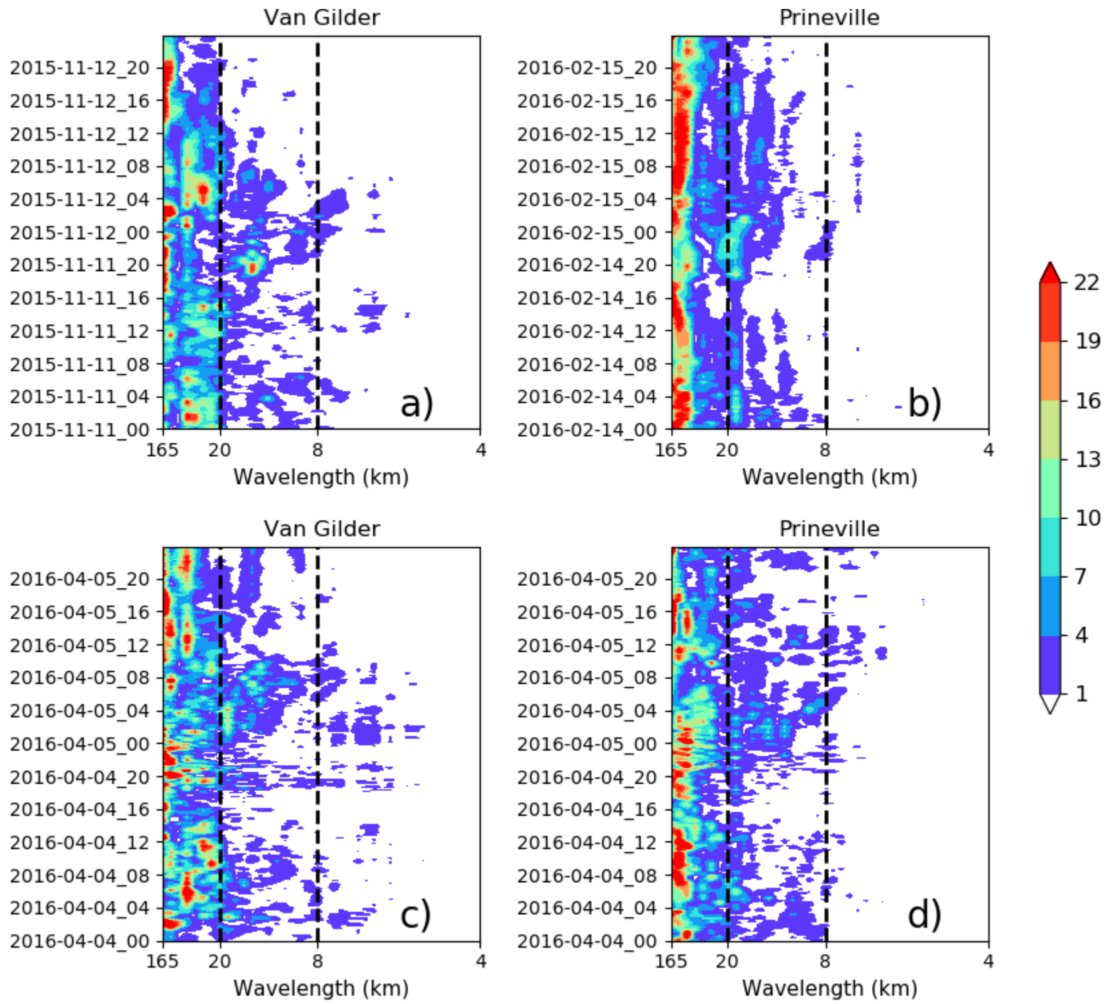

Figure 4: Hovmöller diagram of the power variance (%) with respect to wavelength at the latitude of the targeted station sites: a) Van Gilder, 2015111; b) Prineville, 20160214; c) Van Gilder, 20160404; and d) Prineville, 20160404. The two dotted black lines indicate wavelength at 8 and 20 km.

3.2 Scorer Parameters from model simulations

To determine whether the simulated atmospheric conditions are favorable for generating mountain waves, the Scorer Parameter (SP; Scorer et al., 1949) is computed from the model simulation, where,

$$SP = \frac{N^2}{U^2} - \left(\frac{1}{U}\right)\left(\frac{d^2U}{dz^2}\right) \quad (1)$$

From Eq. (1), the SP is determined by wind speed (U), Brunt–Väisälä frequency (N), and vertical wind shear. This parameter is widely used as an indicator of whether mountain waves, specially the trapped lee waves, can be expected. In general, when the SP is nearly constant with height, conditions are favorable for vertically propagating mountain waves. The trapped lee waves are likely to occur when the SP decreases with height. This is especially true if the decrease of the SP occurs suddenly in the mid-troposphere, dividing the troposphere into two regions, a lower layer with large values (high stability) and an upper layer with small values (low stability; Li et al., 2017).

Figure 5 shows the simulated SP before (blue) and after (red) the targeted wave period for all four mountain wave cases. For the mountain wave event at Van Gilder on 20151111 (Fig. 5a), the SP shows a significant negative slope from the surface to around 400 m AGL both before and after the wave activity, indicating favorable conditions for generating trapped lee waves. Above that, the SP slightly increases or slightly increases than decrease with height. This type of SP profile is also generally true for the mountain wave event at Prineville on 20160214 (Fig. 5b) and Van Gilder on 20160404 (Fig. 5c). The SP from Prineville on 20160404 (Fig. 5d) increases with height from the surface to about 1200 m AGL and then decreases with height both before and after the wave activity. Even though the decrease of SP does not occur near the surface, the implication from the SP profile is the same as the previous cases, suggesting that the background atmospheric conditions are favorable for generating mountain waves, especially the trapped lee waves. Therefore, the simulated atmospheric conditions throughout the targeted wave periods are favorable for trapped lee waves development in all four cases.

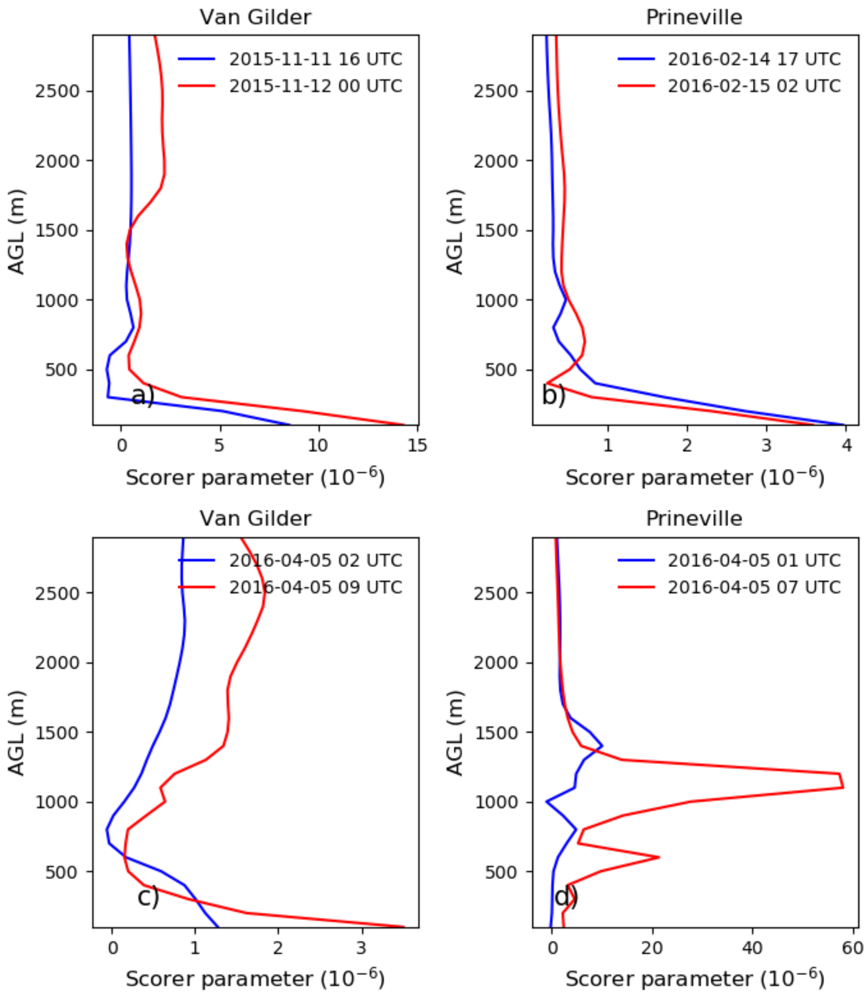

Figure 5: Simulated Scorer Parameter profile in the lowest 3000 m layer from the four mountain wave events: a) Van Gilder, 20151111; b) Prineville, 20160214; c) Van Gilder, 20160404 and d) Prineville, 20160404. The blue (red) line indicates the Scorer parameter before (after) the mountain wave event.

3.3 Validating the simulated mountain wave impact on hub-height wind speed with SoDAR observations.

As discussed in Section 2.2, the simulated hub-height wind speed is reconstructed with respect to the targeted wavelengths (8 ~ 20 km) and wave periods (1 ~ 4 hour). The resulting time series represents the simulated mountain wave impacts on hub-height wind speed. The observed hub-height wind speed is band-pass filtered using the same wave periods (1 ~ 4 hour). The resulting time series indicates the observed wind speed with the same wave period as the simulated mountain waves. By comparing the amplitude of these two timeseries, the correlation between the simulated mountain wave activities and the observed wave pattern at the hub-height level can be assessed.

Figure 6 shows the timeseries of the reconstructed hub-height wind speed between the model (blue) and observations (green) at Van Gilder and Prineville from all four cases. For comparison purposes, the simulated wind speed is only plotted during the period when the significant mountain wave event occurs, whereas the observed wind speed is plotted for a longer period, extending a few hours (~ 5 hours) before and after the event. In general, the magnitude of the simulated wave activities matches well with the observations except at Van Gilder on 20160214. However, there seems to be a time lag in terms of wave pattern between the model and observations in all four cases. Note that Draxl et al., (2020) found that the simulated wind speed due to mountain wave shows a significant correlation with the SoDAR observations after a 1-hour shift for the mountain wave event that happened on September 24th 2016. Therefore, the Pearson correlation coefficient for the timeseries is calculated between the model and observation from -1 to +1 hour for all four events, as shown in Table 2.

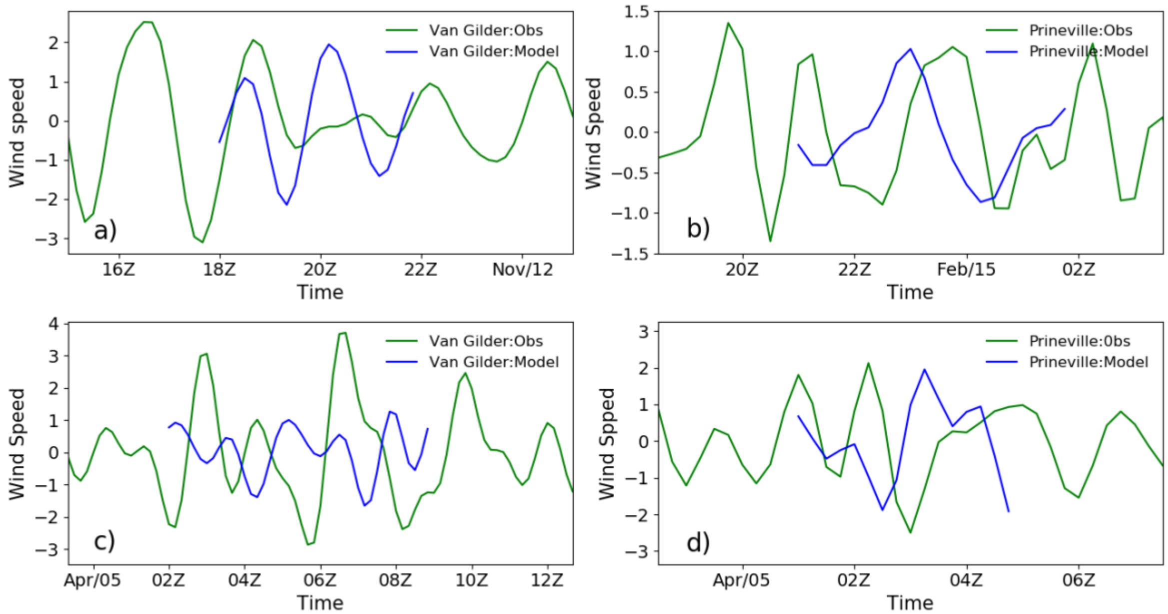

Figure 6: Timeseries of reconstructed hub-height wind speed ($m.s^{-1}$) from SoDAR observation and model simulation. The simulated wind speed (green) is only plotted during the period when the significant mountain wave event occurs, whereas the observed wind speed (red) is plotted for a longer period, extending a few hours (~ 5 hours) before and after the event: a) The green line indicates the observed hub-height wind speed with wave periods from 1 to 4 hour at Van Gilder, 20151111. The blue line indicates the simulated hub-height wind speed with wavelength from 8 to 20 km and wave period from 1 to 4 hour at Van Gilder, 20151111; b) Similar as a) but at Prineville, 20160214; c) Similar to a) but at Van Gilder, 20160404; d) Similar as a) but at Prineville, 20160404.

Table 2: Time Lag Correlation Between Observed and Simulated Hub-Height Wind Speeds From the Three Case Studies

Event \ Time	-60m	-50m	-40m	-30m	-20m	-10m	0	10m	20m	30m	40m	50m	60m
VG 20151111	-0.24	**-0.48**	**-0.56**	**-0.50**	-0.33	-0.07	0.25	**0.47**	**0.47**	0.30	0.05	-0.21	**-0.47**
PR 20160214	0.05	-0.24	**-0.44**	**-0.59**	**-0.63**	**-0.48**	-0.02	**0.48**	**0.74**	**0.74**	**0.53**	0.17	-0.23
VG 20160404	-0.02	-0.11	-0.18	-0.23	**-0.27**	**-0.31**	-0.35	**-0.34**	-0.24	-0.06	0.13	**0.30**	**0.40**
PR 20160404	-0.12	-0.09	0.10	-0.04	**-0.52**	**-0.70**	-0.31	0.18	0.34	0.33	0.43	**0.47**	0.29

*Blue (red) indicates that the correlation is negative (positive). The bold value indicates that the correlation is statically significant at least the 93 % level. 'm' stands for minute.

From -1 to 0 hour (present), more than 90 % of the correlations are negative, suggesting that the simulated mountain wave impact on hub-height wind speed is out of phase with the observations. However, such pattern is drastically reversed to about 75 % being positive correlated from 0 to +1 hour. In addition, there is at least one positive correlation that is statistically significant at the 93% confidence level for each event. Together with Draxl et al., (2020), the results seem to suggest that the WRF model has moderate ability to reproduce the observed mountain wave impacts on hub-height wind speeds. However, the simulated mountain wave impacts tend to occur about an hour earlier than the actual observations.

3.4 Sensitivity to vertical resolution and planetary boundary layer scheme

Two additional experiments are designed to test the sensitivity of our results to vertical resolution and the planetary boundary layer (PBL) scheme. In experiment 1 (EXP1), the number of vertical layers increases from 44 to 65, where the extra levels are mostly added to the boundary layer. In experiment 2 (EXP2), the PBL scheme changes from the Yonsei University scheme (YSU, Hong et al., 2006) to Mellor-Yamada-Nakanishi-Niino (MYNN, Mellor and Yamada., 1982; Nakanishi and Niino., 2009). Note that the land surface physic scheme in EXP2 is also changed to MYNN because the PBL and land surface physic schemes are generally coupled together. Due to high computational expenses in conducting these 750-m resolution simulations, these two experiments are only conducted for the mountain wave case on 20151111.

Figure 7a) and 7b) show similar plots to Figure 6a) but from EXP1 and EXP2 respectively. The corresponding time-lag correlation is also calculated and shown in Table 3. In both experiments, the simulated hub-height wind speed due to mountain waves agrees well with the observations, except that the magnitude of wave activities in EXP1 decreases due to increased vertical resolution. In addition, the time-lag correlation from Table 3 shows very similar results as compared to that from Table 2, suggesting that the simulated mountain wave impacts on hub-height wind speed occur earlier than the actual observations despite changes in vertical resolution and PBL scheme. Note that the correlation coefficients from both experiments are generally more extreme (more negative and more positive) than the original simulation. There could be many possible reasons.

For instance, increasing vertical levels, especially in the boundary layer, might help resolve the vertical mixing as well as turbulent flux transports whereas the MYNN, in this particular case study, might have produced more realistic atmospheric structure than that from the YSU. Nevertheless, these experiments suggest that our result is not very sensitive to the choice of PBL scheme and vertical resolution and MYNN might be a better PBL scheme for simulating impacts of mountain waves on hub-height wind speed.

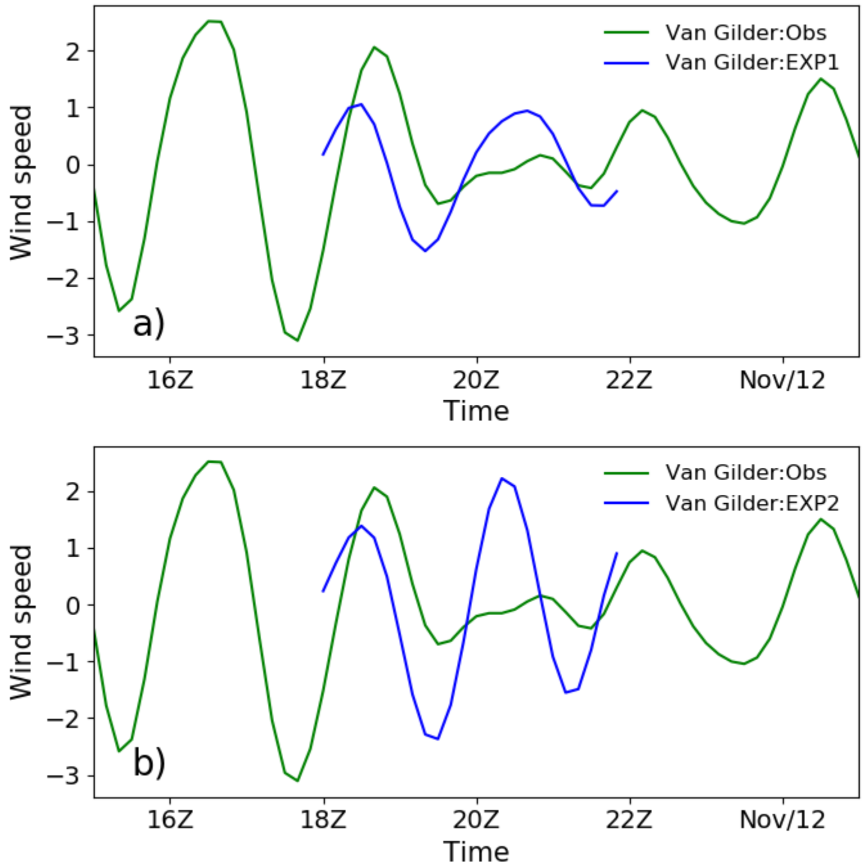

Figure 7: Timeseries of reconstructed hub-height wind speeds from SoDAR observations and model simulation for the 20151111 mountain wave case: both a) and b) are similar to Figure 6a) except that the blue line in a) is from EXP1 where the model vertical levels increase from 44 to 66 and the blue line in b) is from EXP2 where the PBL scheme changes from YSU to MYNN.

Table 3: Time Lag Correlation Between Observed and Simulated Hub-Height Wind Speeds From EXP1 and EXP2

Time / Event	-60m	-50m	-40m	-30m	-20m	-10m	0	10m	20m	30m	40m	50m	60m
VG (EXP1) 20151111	**-0.50**	**-0.75**	**-0.79**	**-0.67**	**-0.43**	-0.09	0.29	**0.53**	**0.52**	**0.35**	0.14	-0.03	-0.12
VG (EXP2) 20151111	**-0.48**	**-0.68**	**-0.69**	**-0.55**	-0.33	-0.02	0.33	**0.57**	**0.57**	**0.39**	0.13	-0.16	**-0.45**

* Blue (red) indicates that the correlation is negative (positive). The bold value indicates that the correlation is statically significant to at least the 95 % level. In EXP1, the model vertical level changes from 44 to 66. In EXP2, the PBL scheme changes from YSU to MYNN. “m” stands for minute.

4. Uncertainties

4.1 Uncertainty associated with wavelength range

In this study, the simulated mountain wave signals are reconstructed using a wavelength range from 8 to 20 km (Wilczak et al. 2019; Draxl et al. 2020). To justify that our selection of wavelength range is sufficient to capture the simulated mountain wave activities, a similar analysis is performed, in which the simulated hub-height wind speed is reconstructed with wavelength ranges from 20 to 55 km. Note that such analysis is not performed for wavelength smaller than 8 km because the associated power variance is small (Fig. 3).

Figure 8 shows the Hovmöller diagram of simulated hub-height wind speed and reconstructed wind speed at the latitude of Prineville and Van Gilder from all four mountain wave events. Figure 8a), 8d), 8g), 8j) represent the original simulated hub-height wind speed from the model simulation. Figure 8b), 8e), 8h) and 8k) represent the reconstructed hub-height wind speed with wavelength ranging between 8 and 20 km whereas Figure 8c), 8f), 8i) and 8l) represent reconstructed hub-height wind speed with wavelength ranges between 20 and 55km. From the original wind speed plots, we can easily identify the four significant mountain wave events, which are characterized by basin-wide wave patterns and large wind speed. The wind speeds reconstructed with wavelength ranging from 8 to 20 km are able to mostly capture the simulated wave pattern during the mountain wave event. However, such mountain wave-induced wave activities have mostly disappeared for wavelength ranging from 20 to 55km. The results justify that our choice of wavelength range is sufficient to capture most of the simulated mountain wave impacts on hub-height wind speed.

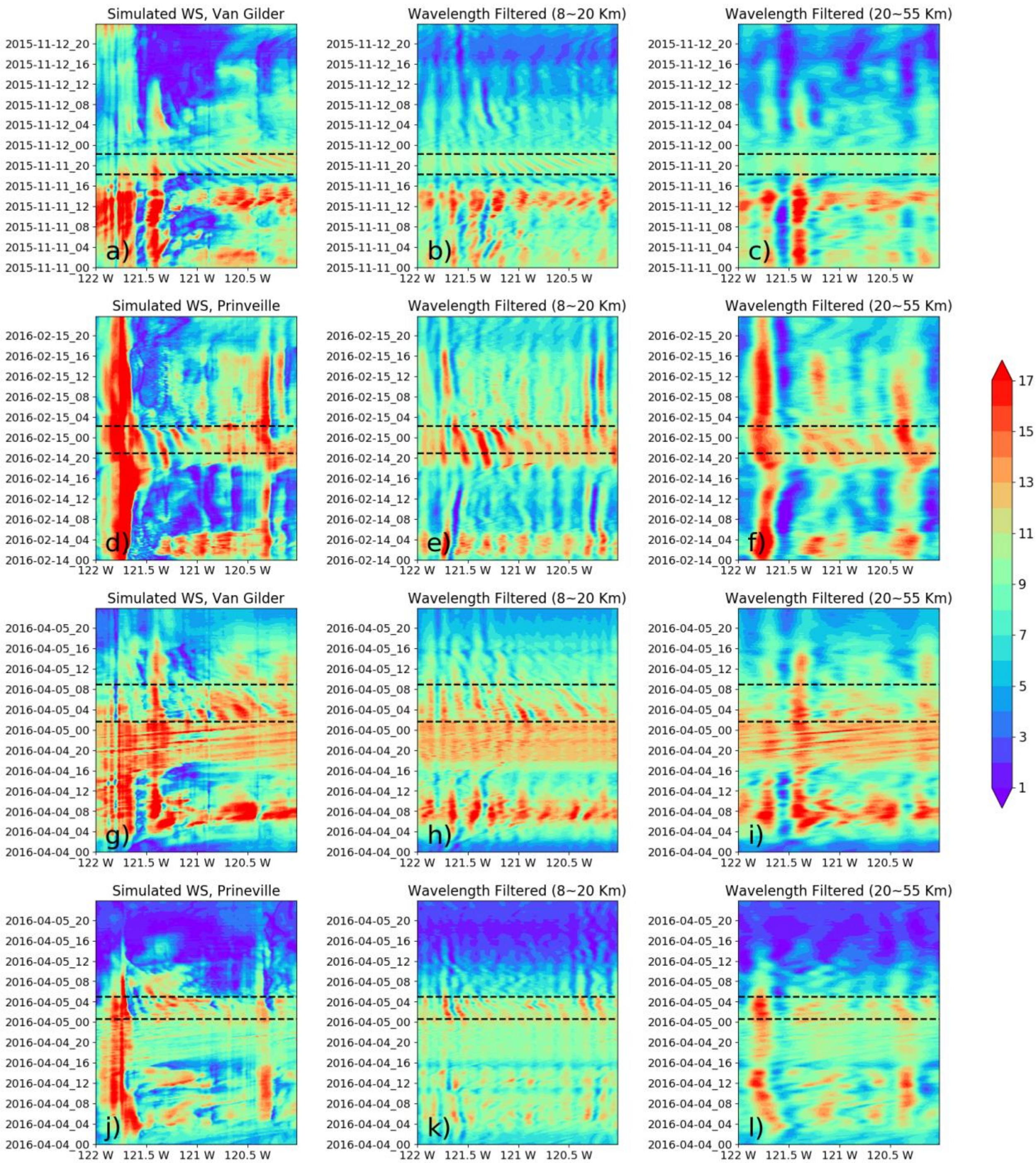

Figure 8: Hovmöller diagram of simulated wind speed at targeted latitude of Van Gilder and Prineville from the three mountain wave simulations: a) original wind speed at Van Gilder from 20151111; b) same as a) but the wind speed is reconstructed with wavelength range from 8 to 20 km; c) same as a) but the wind speed is reconstructed with wavelength range from 20 to 55 km; d) original wind speed at Prineville from 20160214; e) same as d) but the wind speed is reconstructed with wavelength range from 8 to 20 km; f) same as d) but the wind speed is reconstructed with wavelength range from 20 to 55 km; g) original wind speed at Van Gilder from 20160404; h) same

as g) but the wind speed is reconstructed with wavelength range from 8 to 20 km; i) same as g) but the wind speed is reconstructed with wavelength range from 20 to 55 km. j) original wind speed at Prineville from 20160404; k) same as j) but the wind speed is reconstructed with wavelength range from 8 to 20 km; l) same as j) but the wind speed is reconstructed with wavelength range from 20 to 55 km. The black dashed lines indicate the period of significant mountain wave event for each case.

4.2 Uncertainty associated with wave period

To test the uncertainties of our results associated with wave periods, Figure 9 shows a similar plot as Figure 6 but the timeseries is reconstructed with wave periods from 4 to 8 hours, instead of 1 to 4 hours. For the mountain wave case study on 20151111 (Fig. 9a), the magnitude of simulated hub-height wind speed is negligible as compared to the observations. For the mountain wave case study on 20160214, the simulated hub-height wind speeds show a significant positive correlation with the observations between -1 and 0 hour (Fig. 9b), suggesting that low frequency waves might also be important in this particular event. For the mountain wave case study on 20160404 (Fig. 9c and 9d), the simulated hub-height wind speed at both stations show no resemblance with observations. Overall, there is much less consensus in terms of both wave pattern and magnitude between the model and observations when the wave period increases. This could mostly be attributed to the fact that mountain waves, specially trapped lee waves, are high frequency signals. Therefore, reconstructing this type of wave with large wave periods might not be accurate.

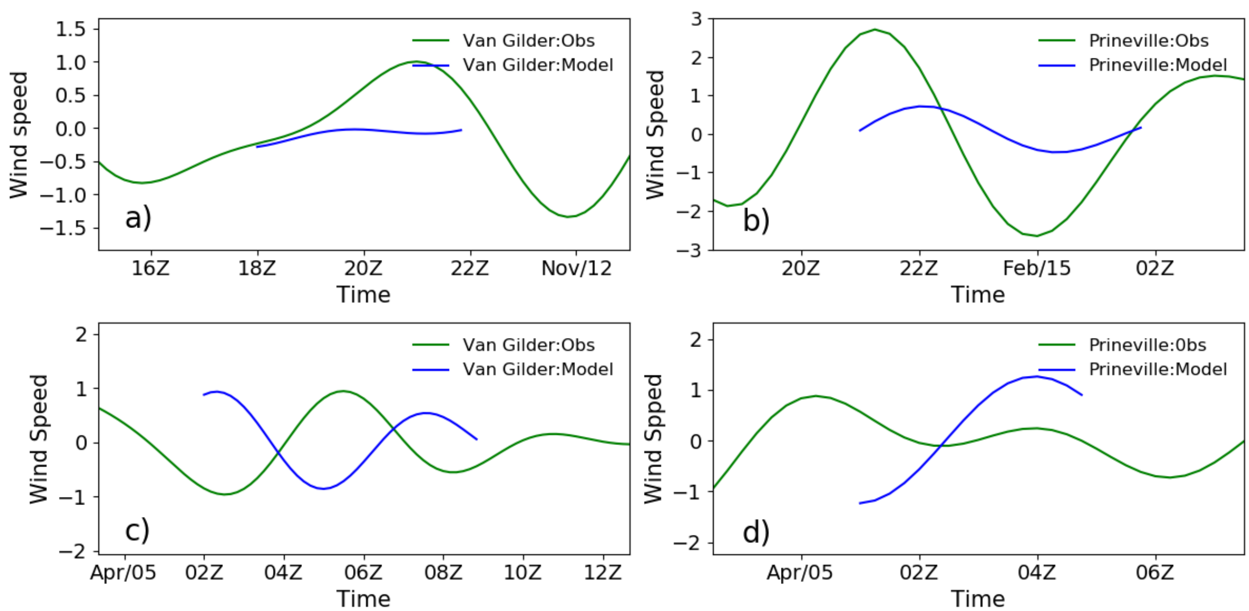

Figure 9: Similar to Figure 6 but both the observed and simulated timeseries are reconstructed with wave period from 4 to 8 hour.

4.3 Uncertainty associated with power variance threshold and wave duration

Other than the selected wavelength range and wave period, the other two important factors in this analysis are the 25 % threshold value and the 3-hour duration which are used to determine the significant mountain wave events (Figure 3). Most certainly, if the threshold value decreases or increases, both the length and number of these significant mountain wave events will change. For instance, if the threshold decreases to 20 %, there will be another simulated mountain wave event from November 12th 04Z to November 12th 08Z for 20151111 case. However, this simulated mountain wave event is much weaker compared to the first event (Fig. 8a). Note that in this study, we are only interested in significant mountain wave activities and our current threshold value certainly can capture such major mountain wave activities from all three case studies.

Similarly, if the wave duration increases, there will be fewer simulated mountain wave events to examine. In that case, the significant but relative short mountain wave event, such as that happened on 20151111 (Fig. 3a) will be left out. On the other hand, if the wave duration decreases to 1 hour, the number of simulated mountain wave event will increase drastically. However, the relatively short data period might not be sufficient to establish any statistically significant relationship between the observations and model simulations.

In order to determine a more accurate threshold value for significant mountain wave's intensity and duration, more collaborations between the scientific community and the wind energy sector are needed to examine how big the impact does real-world mountain wave have on the actual wind power production. Only then, we can have more confidence in issuing hazard warning when such mountain wave activities are forecasted.

5. Summary and conclusions

Recent studies (Wilczak et al. 2019; Draxl et al. 2020) have shown that mountain wave activity impacts wind power generation. While predicting the exact details of mountain waves might be difficult, it is still valuable to evaluate a numerical model's ability to simulate such events. In this study, we applied FFT to extract the simulated mountain wave signals on hub-height wind speed from three mountain wave simulations, using band-pass filtering, and compared with SoDAR observations. These three mountain wave events were identified as being of significant importance to the wind energy sector by the WFIP2 team.

Our results suggest that the WRF model has moderate skill in simulating observed mountain wave. Further, given WRF predictions of wavelength range and wave period, the FFT can calculate the simulated mountain wave impact on hub-height wind speed. The resulting wind speeds agree well with SoDAR observations in terms of both magnitude and pattern. Finally, for the simulated cases, WRF consistently predicts impacts of significant mountain wave events about an hour earlier than the actual observations.

There are many possible reasons as to why the simulated mountain wave impact occurs a bit earlier than the observation. It is possible that the band-pass filtering does not capture the entire spectrum of simulated mountain wave activities. In addition, misrepresentation from the prescribed initial conditions as well as limitation from the model physics, such as the turbulent mixing induced from the PBL scheme, could also be playing a major role. By inheriting the abundance of the WFIP2 observational dataset, we can further explore the cause for this discrepancy, which will be the focus of a subsequent study.

Acknowledgments

The authors thank the WFIP2-experiment participants who aided in the deployment and the collection of remote sensing data as well as our colleagues who monitored, quality controlled and provided data to the Data Archive and Portal (DAP). The research was performed using computational resources sponsored by the Department of Energy's Office of Energy Efficiency and Renewable Energy and located at the National Renewable Energy Laboratory. Julie K. Lundquist’s effort was partially supported by the National Science Foundation under grant AGS-1565498.

This work was authored in part by the National Renewable Energy Laboratory, operated by Alliance for Sustainable Energy, LLC, for the U.S. Department of Energy (DOE) under Contract No. DE-AC36-08GO28308. Funding was provided by the U.S. Department of Energy Office of Energy Efficiency and Renewable Energy Wind Energy Technologies Office. The views expressed in the article do not necessarily represent the views of the DOE or the U.S. Government. A portion of the research was performed using computational resources sponsored by the Department of Energy's Office of Energy Efficiency and Renewable Energy and located at the National Renewable Energy Laboratory.

Data Availability:

Datasets related to this article can be found at: https://data.mendeley.com/datasets/x6hv4nw8yh/draft?a=37141db0-1a13-4bdc-94b1-94381c54e8b1

References:

AMS Glossary: Mountain Wave, http://glossary.ametsoc.org/wiki/Mountain_wave

Bergland GD (1969) A guided tour of the fast Fourier transform. *IEEE Spectrum, 6*, 41-51.

Borkowski J (1969) Spectra of anisotropic turbulence in the atmosphere. Proceedings of Colloquium on Spectra of Meteorological Variables, Stockholm, June 9-19, 1969. *Radio Science*, 4, 1351-1355.

Bianco L, Djalalova IV, Wilczak JM, Olson JB, Kenyon JS, Choukulkar A, Berg LK, Fernando HJS, Grimit EP, Krishnamurthy R, Lundquist JK, Muradyan P, Pekour MS, Pichugina Y, Stoelinga MT, Turner DD (2019) Impact of model improvements on 80-m wind speeds during the second Wind Forecast Improvement Project (WFIP2), Geosci. Model Dev. Discuss., 10.5194/gmd-2019-80

Chen F and Dudhia J (2001) Coupling an advanced land-surface/ hydrology model with the Penn State/ NCAR MM5 modeling system. Part I: Model description and implementation. Mon. Wea. Rev., 129, 569–585.

Dee, DP, Uppala SM, Simmons AJ, Berrisford P, Poli P, Kobayashi S, Andrae U, Balmaseda MA, Balsamo G, Bauer P, Bechtold P, Beljaars ACM, Berg LVD, Bidlot J, Bormann N, Delsol C, Dragni R, Fuentes M, Geer AJ, Haimberger L, Healy SB, Hersbach H, Hólm EV, Isaksen L, Kållberg P, Köhler M, Matricardi M, Mcnally AP, Monge-Sanze BN, Morcrette JJ, Park BK, Peubey C, de Ronsnay P, Tavolato C, Thépaut JN, Vitart F, (2011): The ERA-Interim reanalysis: Configuration and performance of the data assimilation system. *Quart. J. Roy. Meteor. Soc.*, **137**, 553–597, doi:https://doi.org/10.1002/qj.828

Draxl C, Worsnop RP, Xia G, Pichugina Y, Chand D, Lundquist JK, Sharp J, Wedam G, Wilczak JM, Berg LK (2020) Mountain Waves Impact Wind Power Generation. *Wind Energy Science*, Revised

Durran, DR (2003) Lee waves and mountain waves. 10.1016/B0-12-227090-8/00202-5.

Durran, DR (2015) Mountain Meteorology. Lee Waves and Mountain Waves, Encyclopedia of Atmospheric Sciences (Second 490 Edition). Academic Press, pp 95-102, ISBN 9780123822253, https://doi.org/10.1016/B978-0-12-382225-3.00202-4.

DOE, 2018a: Today in energy. Energy Information Administration, accessed 10 May 2019, www.eia.gov /todayinenergy/detail.php?id=35412.

Emeis S, Kalthoff N, Adler B, Pardyjak E, Paci A, Junkermann W (2018) High-Resolution Observations of Transport and Exchange Processes in Mountainous Terrain. *Atmosphere*, *9*, 457.

Feltz WF, Bedka KM, Otkin JA, Greenwald T, Ackerman SA (2009) Understanding satellite-observed mountain wave signatures using high-resolution numerical model data Weather Forecast., 24 (2009), pp. 76-86

Hong, SY, Noh Y, and Dudhia J (2006) A new vertical diffusion package with an explicit treatment of entrainment processes. Mon. Wea. Rev., 134, 2318–2341.

Iacono, MJ, Delamere JS, Mlawer EJ, Shephard MW, Clough SA, Collins WD, (2008) Radiative forcing by long-lived greenhouse gases: Calculations with the AER radiative transfer models, J. Geophys. Res., 113, D13103, doi:10.1029/2008JD009944.

Jimenez, P, Dudhia J, Gonzalez-Ruoco JF, Navarro J, Montavez JP, Garcia-Bustamente E (2012) A revised scheme for the WRF surface layer formulation. Mon. Wea. Rev., 140, 898–918.

Jenkins GM and Watts DG (1968): *Spectral Analysis and Its Applications,* Holden- Day, Oakland, CA. 523pp.

Li L and Chen Y (2017) Numerical simulations of two trapped mountain lee waves downstream of Oahu. *Journal of Applied Meteorology and Climatology*, **56**(5), 1305– 1324.

Lehner M and Rotach MW (2018) Current challenges in understanding and predicting transport and exchange in the atmosphere over mountainous terrain. *Atmosphere*, **9**, 276

Mellor GL and Yamada T (1982) Development of a turbulence closure model for geophysical fluid problems. Rev. Geophys., 20, 851–875

Nakanishi M and Niino H (2009) Development of an improved turbulence closure model for the atmospheric boundary layer. J. Meteor. Soc. Japan, 87, 895–912

Olson, JB, Kenyon JS, Djalalova I, Bianco L, Turner DD, Pichygina Y, Choukulkar A, Toy MD, Brown JM, Angevine WM, Akish E, Bao JW, Jimenez P, Kosovic B, Lundquist KA, Draxel C, Lundquist JK, McCaa J, McCaffrey K, Lantz K, Long C Wilczak J, Banta R, Marquis M, Redfern S, Berg LK, Shaw W, Cline J, (2019) Improving wind energy forecasting through numerical weather pre- diction model development. *Bull. Amer. Meteor. Soc.*, https://doi.org/10.1175/BAMS-D-18-0040.1

Panofsky HA and Brier GW, (1968): *Some Applications of Statistics 10 Meteorology,* Penn State Univ., University Park, PA. 224pp.

Powers, JG, Klemp JB, Skamarock WC, Davis CA, Dudhia J, Gill DO, Coen JL, Gochis DJ, Ahmadov R, Pechham SE, Grell GA, Michalskes J, Trahan S, Benjamin SG, Alexander CR, Dimego GJ, Wang W, Schwartz CS, Romine GS, Liu ZQ, Snyder C, Chen F, Barlage MJ, Yu W, Duda MG, (2017): The Weather Research and Forecasting Model: Overview, system efforts, and future directions. *Bull. Amer. Meteor. Soc.*, **98**, 1717-1737, https://doi.org/10.1175/BAMS-D-15-00308.1.

Raghavendra A, Roundy PE, Zhou LM (2019) Trends in tropical wave activity from the 1980s to 2016. *Journal of Climate*, **32**, 1661– 1676. https://doi.org/10.1175/JCLI-D-18-0225.1.

Stull, R.B., (1998) Introduction to Boundary-Layer Meteorology, *Kluwer Academic Publishers, Dordrecht*, p. 666

Shaw WJ, Berg LK, Cline J, Draxl C, Djalalova I, Grimit EP, Lundquist, JK, Marquis M, McCaa J, Olson, JB, Sivaraman C, Sharp J, Wilczak, JM (2019) The Second Wind Forecast Improvement Project (WFIP 2): General Overview. *Bull. Amer. Meteor. Soc.,* **100**, 1687–1699, https://doi.org/10.1175/BAMS-D-18-0036.1.

Sussman H, Raghavendra A, Roundy PE, Dai A (2020) Trends in northern midlatitude atmospheric wave power from 1950 to 2099, *Climate Dynamics*, 54, 2903-2918

Skamarock, WC, and Klemp JB (2008) A time-split non-hydrostatic atmospheric model for weather research andforecasting applications.J. Comput. Phys.,227, 3465–3485

Scorer, RS (1949) Theory of waves in the lee of mountains. Q. J. R. Meteorol. Soc., 75: 41-56. doi:10.1002/qj.49707532308.

Serafin S, Adler B, Cuxart J, De Wekker SFJ, Gohm A, Grisogono B, Kalthoff N, Kirshbaum DJ, Rotach MW, Schmidli J (2018) Exchange processes in the atmospheric boundary layer over mountainous terrain. *Atmosphere, 9*, 102.

Thompson G, Field PR, Rasmussen RM, Hall WD, (2008) Explicit Forecasts of Winter Precipitation Using an Improved Bulk Microphysics Scheme. Part II: Implementation of a New Snow Parameterization. Mon. Wea. Rev., 136, 5095–5115.

Thompson G and Eidhammer T, (2014) A study of aerosol impacts on clouds and precipitation development in a large winter cyclone. J. Atmos. Sci., 71, 3636–3658.

Vaisala, 2015: Triton remote sensing systems: Comparing accuracy with collocated met towers. Vaisala white paper, available from: https://www.vaisala.com/en/industries-innovation/renewable-energy-and-weather.

Veers P, Dykes K, Lantz E, Barth S, Bottasso CL, Carlson O, Clifton A, Green J, Green P, Holttinen H, Laird D, Lehtomäki V, Lundquist JK, Manwell J, Marquis M, Meneveau C, Moriarty P, Munduate X, Muskulus M, Naughton J, Pao L, Paquette J, Peinke J, Robertson A, Rodrigo JS, Sempreviva AM, Smith JC, Tuohy A, Wiser R, (2019) Grand challenges in the science of wind energy. *S*cience, **366**, 6464.

van den Bossche M and De Wekker SFJ (2019) Representativeness of wind measurements in moderately complex terrain. *Theor Appl Climatol* **135,** 491–504. https://doi.org/10.1007/s00704-018-2402-z

Vermote EF, Kotchenova SY, Ray JP.(2015) MODIS surface reflectance user's guide. MODIS Land Surface Reflectance Science Computing Facility, version 1.4

Wilczak JM, Stoelinga M, Berg LK, Sharp J, Draxl C, McCaffrey K, Banta RM, Bianco L, Djalalova I, Lundquist JK, Muradyan P, Choukulkar A, Leo L, Bonin T, Pichugina Y, Eckman R, Long CN, Lantz K, Worsnop RP, Bickford J, Bodini N, Chand D, Clifton A, Cline J, Cook DR, Fernando HJ, Friedrich K, Krishnamurthy R, Marquis M, McCaa J, Olson JB, Otarola-Bustos S, Scott G, Shaw WJ, Wharton S, White AB, (2019) The Second Wind Forecast Improvement Project (WFIP 2): Observational Field Campaign. *Bull. Amer. Meteor. Soc.*, **100**, 1701–1723, https://doi.org/10.1175/BAMS-D-18-0035.1.

Xia G, Cervarich M, Baidya SB, Zhou L, Minder J, Freedam JM, Jiménez PA (2017) Simulating impacts of real-world wind farms on land surface temperature using WRF model: validation with MODIS observations. Mon Weather Rev 145:4813–4836

Xia G, Zhou L., Minder JR, Fovell RG, Jimenez PA (2019) Simulating impacts of real-world wind farms on land surface temperature using the WRF model: physical mechanisms, Clim. Dyn., 53 (2019), pp. 1723-1739